THE JOURNAL OF PHYSICAL CHEMISTRY B
A JOURNAL OF THE AMERICAN CHEMICAL SOCIETY

pubs.acs.org/JPCB

Article

Electroosmotic Flow in Polarizable Charged Cylindrical Nanopores

Published as part of The Journal of Physical Chemistry virtual special issue "Dor Ben-Amotz Festschrift".

Rogério K. Bombardelli,* Igor M. Telles,* Alexandre P. dos Santos,* and Yan Levin*

Cite This: *J. Phys. Chem. B* 2021, 125, 11091−11098

Read Online

ACCESS | Metrics & More | Article Recommendations | Supporting Information

ABSTRACT: We present a simulation method to study electroosmotic flow in charged nanopores with dielectric contrast between their interior and the surrounding medium. To perform simulations, we separate the electrostatic energy into the direct Coulomb and the polarization contributions. The polarization part is obtained using periodic Green functions and can be expressed as a sum of fast converging modified Bessel functions. On the other hand, the direct Coulomb part of the electrostatic energy is calculated using fast converging three-dimensional (3D) Ewald summation method, corrected for a pseudo one-dimensional (1D) geometry. The effects of polarization are found to be particularly important for systems with multivalent counterions and narrow nanopores. Depending on the surface charge density, polarization can increase the volumetric flow rate by 200%. For systems with 3:1 electrolyte, we observe that there is a saturation of the volumetric flow rate. In this case, for polarizable pores, the flow rate is 100% higher than for nonpolarizable pores.

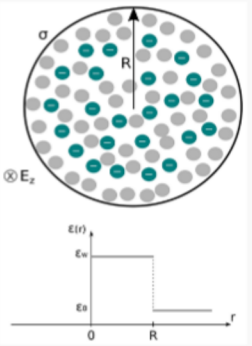

INTRODUCTION

Confined electrolytes are encountered in various realms of life sciences and engineering. A particularly important example is ionic transport through nanopores,[1−3] such as ion channels.[4−7] The industrial applications range from energy conversion[8−10] and ion electronics,[11,12] to supercapacitors[13,14] and ionic biosensors.[15,16] The electroosmosis occurs when an electric field is applied to a confined electrolyte solution. The fluid flows when the counterions—released from the surface groups or from the added salt—move under the action of the external electric field, in the process dragging the surrounding solvent. The electroosmotic flows are often present in chemical and biological systems.[17,18] They are used in soil treatment,[19,20] chemical analysis,[21−23] and DNA electrophoresis.[24−26] The electroosmotic flows are also being used in microfluidic devices,[27−29] ionic circuits,[30] and in the diagnosis of viral infections.[31]

Generally, surfaces and interfaces separate mediums of different dielectric permittivity. This is the case for biological membranes and colloidal particles, which have a dielectric constant much smaller than the surrounding water. In the presence of external charge, the dielectric contrast results in the polarization of the interface and the induced surface charge, which generally is inhomogeneously distributed over the interface. Surface polarization, on the microscale and nanoscale, plays an important role[32−40] in colloidal suspensions,[41,42] polyelectrolyte capacitors,[43] polyelectrolyte brushes,[44,45] and biological membranes. Besides the electrostatic correlations,[46,47] the electroosmotic flow is also strongly influenced by the polarization of confining surfaces in a planar double-slit channel.[48] Recent works also show that electrokinetic phenomena can be affected by solvent and ionic polarizabilities[49] and that curvature effects can be very important.[50] In a recent work, the electroosmotic flows were studied in cylindrical geometry using a three-dimensional (3D) Ewald summation method corrected for a pseudo one-dimensional (1D) geometry.[51] In the present paper, we will extend this approach to account for the surface polarization of the nanopores, which generally pass through a low dielectric medium, such as a cell membrane. Our approach relies on solution of the Poisson equation using periodic Green functions. In this way, we are able to separate the polarization contribution to the overall electrostatic potential from the direct Coulomb interaction between the ions. The direct Coulomb interaction can then be treated using a 3D Ewald summation, corrected for a pseudo 1D geometry, while polarization contribution can be expressed in terms of a rapidly converging series of modified Bessel functions. We apply the new method to simulate the electroosmotic fluid flow through a polarizable cylindrical nanopore using the Dissipative Particle Dynamics (DPD) method.[52] Our goal is to obtain the volumetric flow rates (VFR) for pores with different surface charge and electrolyte concentrations.

The paper is organized as follows. In the first section, the model and the DPD method are explained. In the following

Received: July 30, 2021
Revised: September 9, 2021
Published: September 27, 2021

https://doi.org/10.1021/acs.jpcb.1c06783
J. Phys. Chem. B 2021, 125, 11091−11098

section, the electrostatic energy is calculated. The next section presents the results, and the last section discusses the conclusions of the present work.

THE MODEL

The model system is represented in Figure 1. It consists of N_{sol} solvent (number N_{sol}) and charged particles (number N)

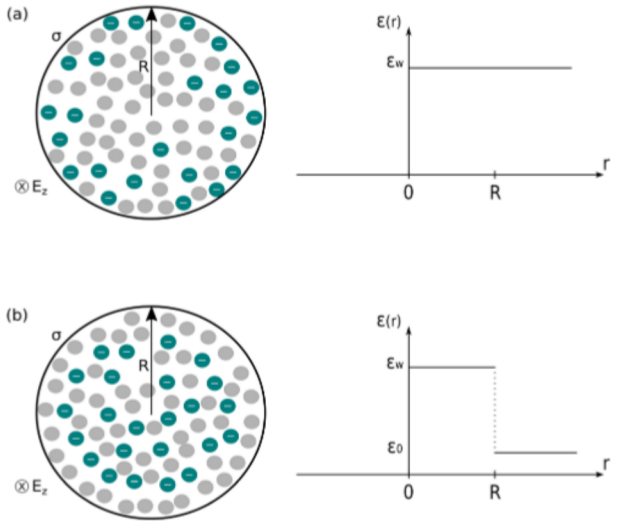

Figure 1. Schematic illustration of the system: (a) homogeneous–nonpolar pore and (b) polarizable pore. Solvent particles and ions are confined in an infinite charged pore of surface charge density σ and radius R, oriented along the z-axis. The right-hand side of the figure shows the dielectric profiles inside and outside the pore.

confined in a cylinder of uniform surface charge density σ ($\sigma < 0$), of radius R and length L. Among the charged particles, there are N_c counterions derived from the ionization of surface groups, and N_+ counterions and N_- co-ions derived from the dissociation of salt. The number of surface-derived counterions is $N_c = \sigma 2\pi RL/\alpha e$, where α is the counterion valence and e is the elementary charge. The number of salt particles is determined by the concentration of salt (ρ_s) inside the pore. The number of solvent particles (N_{sol}) is determined by their concentration (n_{sol}). The interactions between all of the particles are governed by the DPD forces.[52−54] The DPD method uses three forces—conservative, dissipative, and random—in addition to electrostatic and Lennard-Jones interactions between the charged particles. The forces act together in a way to satisfy the fluctuation−dissipation theorem and the conservation of momentum. The DPD parameters used in this work are the same as those presented in refs 51 and 52. The ions have a central charge and all particles have the same mass m. The dynamics is performed inside a cylinder with periodic boundary condition in the z-direction and no-slip boundary condition at $r = R$, enforced by the bounce-back technique.[55] The electric field is applied in the z direction with magnitude $E_z = 1\ (e\beta l_B)^{-1}$. The natural units used in the simulations are mass m, inverse thermal energy β ($\beta = 1/k_BT$), and the Bjerrum length l_B ($l_B = e^2/\varepsilon_w k_B T$, where $\varepsilon_w = 80$ is the water dielectric constant, k_B the Boltzmann constant, and T the temperature. To account for the hard core of ions, a regular truncated Lennard-Jones potential is used with a minimal distance of $0.5\ l_B$ and strength $\beta\epsilon = 0.5$. The DPD forces between particles i and j are given by the conservative force ($\mathbf{F}_{ij}^C$, eq 1), the dissipative force ($\mathbf{F}_{ij}^D$, eq 2), and the random force ($\mathbf{F}_{ij}^R$, eq 3):

$$\mathbf{F}_{ij}^C = \begin{cases} a_{ij}\left(1 - \dfrac{|\mathbf{r}_{ij}|}{r_c}\right) & \text{if } |\mathbf{r}_{ij}| \le r_c \\ 0 & \text{if } |\mathbf{r}_{ij}| > r_c \end{cases} \tag{1}$$

$$\mathbf{F}_{ij}^D = \begin{cases} -\gamma w_D(|\mathbf{r}_{ij}|)(\hat{\mathbf{r}}_{ij}\cdot\mathbf{v}_{ij}) & \text{if } |\mathbf{r}_{ij}| \le r_c \\ 0 & \text{if } |\mathbf{r}_{ij}| > r_c \end{cases} \tag{2}$$

$$\mathbf{F}_{ij}^R = \begin{cases} \dfrac{\xi}{\sqrt{\Delta t}}\zeta_{ij} w_R(|\mathbf{r}_{ij}|)\hat{\mathbf{r}}_{ij} & \text{if } |\mathbf{r}_{ij}| \le r_c \\ 0 & \text{if } |\mathbf{r}_{ij}| > r_c \end{cases} \tag{3}$$

The coefficients a_{ij} are set to 0, 0, and 20 $(\beta l_B)^{-1}$ for ion−ion, ion−solvent, and solvent−solvent interactions, respectively. The separation and relative velocity vectors between particles i and j are $\mathbf{r}_{ij}$ and $\mathbf{v}_{ij}$. The interaction amplitudes are $w_R(|\mathbf{r}_{ij}|) = (1 - |\mathbf{r}_{ij}|/r_c)$ and $w_D(|\mathbf{r}_{ij}|) = w_R(|\mathbf{r}_{ij}|)^2$, with the cutoff radius set to $r_c = l_B$, and parameters $\gamma = 4.5\ (m/\beta)^{0.5} l_B^{-1}$ and $\xi^2 = 2\gamma k_B T$, while ζ_{ij} is a uniformly distributed random number with zero mean and unit variance. The forces are constructed to satisfy the fluctuation−dissipation theorem.[52−54] The electrostatic force acting on an ion is calculated from the derivative of electrostatic energy,[51] which is presented in the following section. The integration of equations of motion is performed using the velocity−Verlet algorithm.

ELECTROSTATIC ENERGY

Computer simulations are performed using a relatively small number of particles inside a fairly small simulation cell. Unlike that observed for systems with short-range interactions, for systems with long-range, such as Coulombic, one cannot use simple periodic boundary conditions. Instead, a rectangular simulation cell of dimensions $L_p \times L_p \times L$ must be periodically replicated to account for the long-range interaction between the distant particles. To model a long cylindrical pore, a periodic replication must be performed only in the z-direction. Consider N charges q_i confined inside a cylinder of radius R and length L, placed along the main axis of the simulation cell. Inside the cylinder, the dielectric medium is uniform with relative dielectric constant ε_w, while outside the pore, the relative dielectric constant is ε_o. The electrostatic potential, the Green function, produced by a periodically replicated point charge located at $\mathbf{r}_i = (\rho_i, \theta_i, z_i)$ inside a cylindrical pore satisfies the Poisson equation,

$$\nabla^2 G(\mathbf{r};\ \mathbf{r}_i) = -\frac{4\pi q_i}{\varepsilon_w}\sum_{m=-\infty}^{+\infty}\delta(\mathbf{r} - \mathbf{r}_i - mL\hat{\mathbf{z}}) \tag{4}$$

where the coordinate of the observation point is $\mathbf{r} = (\rho, \theta, z)$. The delta functions can be expressed as

$$\sum_{m=-\infty}^{+\infty}\delta(\mathbf{r} - \mathbf{r}_i - mL\hat{\mathbf{z}}) = \frac{1}{\rho}\delta(\rho - \rho_i)\frac{1}{2\pi L}\sum_{m=-\infty}^{+\infty}\cos[m(\theta - \theta_i)]\sum_{n=-\infty}^{+\infty}\cos[k_n(z - z_i)] \tag{5}$$

where $k_n = 2\pi n/L$. Writing the Green function as

https://doi.org/10.1021/acs.jpcb.1c06783
J. Phys. Chem. B 2021, 125, 11091−11098

$$G(\mathbf{r};\mathbf{r}_i) = \frac{g(\rho;\rho_i)}{2\pi L}\sum_{m=-\infty}^{+\infty}\sum_{n=-\infty}^{+\infty}\cos[m(\theta-\theta_i)]\cos[k_n(z-z_i)] \quad (6)$$

and substituting into eq 4, we find that[56]

$$g(\rho;\rho_i) = \frac{4\pi q_i}{\varepsilon_w} I_m(k_n\rho_<)[K_m(k_n\rho_>) + \gamma_{mn} I_m(k_n\rho_>)] \quad (7)$$

where $\rho_>$ and $\rho_<$ are the larger and the smaller values of the radial positions $\{\rho,\rho_i\}$,

$$\gamma_{mn} = \frac{K_m(k_nR)K_m'(k_nR)(\varepsilon_o-\varepsilon_w)}{\varepsilon_w I_m'(k_nR)K_m(k_nR) - \varepsilon_o I_m(k_nR)K_m'(k_nR)} \quad (8)$$

and $I_m(x)$ and $K_m(x)$ are the modified Bessel functions. Prime symbols ($'$) indicate the derivative of the respective Bessel function.

We note that when the dielectric contrast between the interior and the exterior of the pore vanishes, $\varepsilon_o = \varepsilon_w$, then $\gamma_{mn} = 0$. In this case, $g(\rho;\rho_i)$ reduces to

$$g(\rho;\rho_i) = \frac{4\pi q_i}{\varepsilon_w} I_m(k_n\rho_<)K_m(k_n\rho_>)$$

Substituting this expression into eq 6, we obtain the electrostatic potential of an infinite periodic—with period L—linear array of identical charges q_i, in a homogeneous infinite space of dielectric constant ε_w. The electrostatic potential of such an array is divergent. However, the divergence can be easily renormalized away by subtracting an infinite constant. Nevertheless, the remaining expression is still poorly convergent for small ρ. However, using the modified 3D Ewald summation method, it is possible to rewrite this potential in terms of a fast converging series:[51]

$$G_h(\mathbf{r};\mathbf{r}_i) = \sum_{\mathbf{k}\neq 0}^{\infty}\frac{4\pi q_i}{\varepsilon_w V|\mathbf{k}|^2}\exp\left[-\frac{|\mathbf{k}|^2}{4\kappa_e^2} + i\mathbf{k}\cdot(\mathbf{r}-\mathbf{r}_i)\right] - \frac{\pi q_i}{\varepsilon_w V}[(x-x_i)^2 + (y-y_i)^2] + q_i\frac{\operatorname{erfc}(\kappa_e|\mathbf{r}-\mathbf{r}_i|)}{\varepsilon_w|\mathbf{r}-\mathbf{r}_i|} \quad (9)$$

where $\mathbf{k} = \left(\frac{2\pi}{L_p}\eta_x, \frac{2\pi}{L_p}\eta_y, \frac{2\pi}{L}\eta_z\right)$ are the reciprocal vectors and the η parameters are positive and negative integers (including zero). κ_e is the damping parameter ($\kappa_e = 5/L$), and V is the volume of the simulation box ($V = L_p^2L$). Since this approach is based on 3D Ewald summation, the replication method also creates undesired replicas of the array of charges in both x- and y-directions. Therefore, the rectangular simulation box must have sufficiently large empty space in this direction to avoid the interaction with spurious replicas. This is accomplished by setting $L_p > 4R$. For larger L_p/L, more $\mathbf{k}$-vectors are needed to achieve convergence, without significantly improving the precision of the calculations.

The direct Coulombic interaction between all the charges inside the pore can then be expressed as[37,51]

$$\beta U_h = l_B\left\{\sum_{i=1}^{N}\sum_{j>i}^{N} q_iq_j\frac{\operatorname{erfc}(\kappa_e|\mathbf{r}_{ij}|)}{|\mathbf{r}_{ij}|} + \sum_{\mathbf{k}\neq\mathbf{0}}\frac{2\pi}{V|\mathbf{k}|^2}\exp\left(-\frac{|\mathbf{k}|^2}{4\kappa_e^2}\right)[A(\mathbf{k})^2 + B(\mathbf{k})^2] + \frac{\pi}{V}(M_x^2 + M_y^2 - Q_tG_x - Q_tG_y) - \frac{\kappa_e}{\sqrt{\pi}}\sum_{i=1}^{N} q_i^2\right\} \quad (10)$$

where

$$A(\mathbf{k}) = \sum_{i=1}^{N} q_i\cos(\mathbf{k}\cdot\mathbf{r}_i) \quad (11)$$

$$B(\mathbf{k}) = -\sum_{i=1}^{N} q_i\sin(\mathbf{k}\cdot\mathbf{r}_i) \quad (12)$$

$$M_x = \sum_{i=1}^{N} q_ix_i \quad (13)$$

$$M_y = \sum_{i=1}^{N} q_iy_i \quad (14)$$

$$G_x = \sum_{i=1}^{N} q_ix_i^2 \quad (15)$$

$$G_y = \sum_{i=1}^{N} q_iy_i^2 \quad (16)$$

A uniform pore surface charge can be taken into account using uniformly distributed point sites. However, such an approach introduces a large number of additional surface charges, which must be included together with the real ions into Ewald summation, significantly slowing down simulations.[51] On the other hand, we note that a uniform surface charge results in zero electric field inside an infinite cylindrical pore and, therefore, can be neglected, as far as ion dynamics is concerned.[51] In this case, however, the pore will no longer be charge neutral—there will be a net charge $Q_t = \sum_{i=1}^{N} q_i$ and the usual Ewald summation method for neutral systems must be corrected to account for the lack of charge neutrality in the interior of the pore.[36] This is accomplished with the help of Q_t-dependent terms appearing in eq 10. The implicit surface charge Ewald method[36,51] results in a significant acceleration of simulations and will be used in the present work.

The total Green function inside the pore, $G(\mathbf{r};\mathbf{r}_i) = G_h(\mathbf{r};\mathbf{r}_i) + G_p(\mathbf{r};\mathbf{r}_i)$, can be separated into the direct Coulombic potential $G_h(\mathbf{r};\mathbf{r}_i)$ of the periodic array of charges presented in eq 9, and the polarization potential given by

$$G_p(\mathbf{r};\mathbf{r}_i) = \frac{2q_i}{\varepsilon_wL}\sum_{n=-\infty}^{+\infty}\sum_{m=-\infty}^{+\infty}\gamma_{mn}I_m(k_n\rho)I_m(k_n\rho_i) \times\cos[m(\theta-\theta_i)]\cos[k_n(z-z_i)] \quad (17)$$

Again, there is an infinite constant when $n = m = 0$, which can be renormalized away. Using the symmetry property, $I_{-m}(x) = I_m(x)$ for m integer, the polarization contribution to the overall Green function can be written as

https://doi.org/10.1021/acs.jpcb.1c06783
J. Phys. Chem. B 2021, 125, 11091−11098

$$G_p(\mathbf{r};\mathbf{r}_i) = \frac{2q_i}{\varepsilon_w L}\Bigg\{4\sum_{n=1}^{+\infty}\sum_{m=1}^{+\infty}\gamma_{mn}I_m(k_n\rho)I_m(k_n\rho_i) \times \cos[m(\theta-\theta_i)]\cos[k_n(z-z_i)] + 2\sum_{n=1}^{+\infty}\gamma_{0n}I_0(k_n\rho)I_0(k_n\rho_i)\cos[k_n(z-z_i)] + \sum_{m=1}^{+\infty}\frac{(\varepsilon_w-\varepsilon_o)\rho^m\rho_i^m}{(\varepsilon_w+\varepsilon_o)mR^{2m}}\cos[m(\theta-\theta_i)]\Bigg\} \quad (18)$$

The polarization contribution to the overall electrostatic energy is then $U_p = \sum_{i=1}^{N}\sum_{j=1}^{N} q_j G_p(\mathbf{r}_j;\mathbf{r}_i)/2$. This can be rewritten in terms of functions that involve only sums over the individual particle positions:

$$\beta U_p = \frac{l_B}{L}\Bigg[4\sum_{n=1}^{+\infty}\sum_{m=1}^{+\infty}\gamma_{mn}(f_1(n,m)^2 + f_2(n,m)^2 + f_3(n,m)^2 + f_4(n,m)^2) + 2\sum_{n=1}^{+\infty}\gamma_{0n}(g_1(n)^2 + g_2(n)^2) + \sum_{m=1}^{+\infty}\frac{(\varepsilon_w-\varepsilon_o)}{(\varepsilon_w+\varepsilon_o)m}(h_1(m)^2 + h_2(m)^2)\Bigg] \quad (19)$$

where

$$f_1(n,m) = \sum_{i=1}^{N} q_i I_m(k_n\rho_i)\cos[m\theta_i]\cos[k_n z_i]$$

$$f_2(n,m) = \sum_{i=1}^{N} q_i I_m(k_n\rho_i)\cos[m\theta_i]\sin[k_n z_i]$$

$$f_3(n,m) = \sum_{i=1}^{N} q_i I_m(k_n\rho_i)\sin[m\theta_i]\cos[k_n z_i]$$

$$f_4(n,m) = \sum_{i=1}^{N} q_i I_m(k_n\rho_i)\sin[m\theta_i]\sin[k_n z_i]$$

$$g_1(n) = \sum_{i=1}^{N} q_i I_0(k_n\rho_i)\cos[k_n z_i]$$

$$g_2(n) = \sum_{i=1}^{N} q_i I_0(k_n\rho_i)\sin[k_n z_i]$$

$$h_1(m) = \sum_{i=1}^{N} q_i\left(\frac{\rho_i}{R}\right)^m\cos[m\theta_i]$$

$$h_2(m) = \sum_{i=1}^{N} q_i\left(\frac{\rho_i}{R}\right)^m\sin[m\theta_i] \quad (20)$$

This significantly facilitates the application in simulations, allowing for an easy update of both energy and force, when the position of a particle changes, without the need to recalculate the whole energy function. The number of n and m terms in summation is dependent on the periodicity of the cylinder, for example, for $L = 10l_B$, we use 10 terms for n and for m, whereas for $L = 70l_B$, we use 40 for both. The derivation of polarization force is given in the Supporting Information.

RESULTS

We start by studying pores with only monovalent counterions, $\alpha = 1$. The pore radius is fixed at $R/l_B = 5$ and the number of counterions at $N_c = 60$. The solvent concentration is fixed at $n_s = 6/l_B^3$. The uniform surface charge density of the pore is σ. The length of the simulation cell is then determined from the charge neutrality, $L = N_c\alpha e/2\pi R\sigma$. For homogeneous pores with $\varepsilon_o = \varepsilon_w$, and for polarizable pores with $\varepsilon_o = 2$, the reduced counterion radial density profiles, $\tilde{\rho}(r) = l_B^3\rho(r)$, are presented in Figure 2

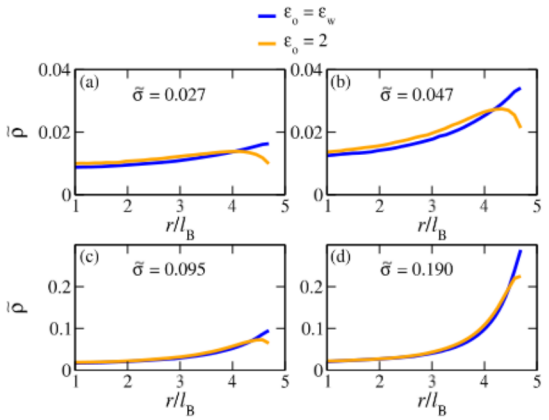

Figure 2. Monovalent counterion density profiles for pores of various surface charge densities. The periodic length L in each panel is $70l_B$, $40l_B$, $20l_B$, and $10l_B$, respectively, and the number of counterions inside one period is $N_c = 60$. The pore radius is $R/l_B = 5$. Blue and orange curves correspond to homogeneous (no dielectric discontinuity) and polarizable ($\varepsilon_w = 80$ and $\varepsilon_o = 2$) cases, respectively.

for reduced pore surface charge density, $\tilde{\sigma} = l_B^2\sigma/e$. We see that the induced surface charge leads to a small repulsion of monovalent counterions from the surface of the pore. However, the effect is small and we do not expect it to strongly affect the electroosmotic flow. Indeed, this is what we observe in DPD simulations, the results of which are presented in Figure 3, using reduced velocity $\tilde{v}$ ($\tilde{v} = \sqrt{m\beta}v$).

We next explore pores with trivalent counterions ($\alpha = 3$). To have the same surface charge density as in the case of monovalent counterions, we fix the number of trivalent

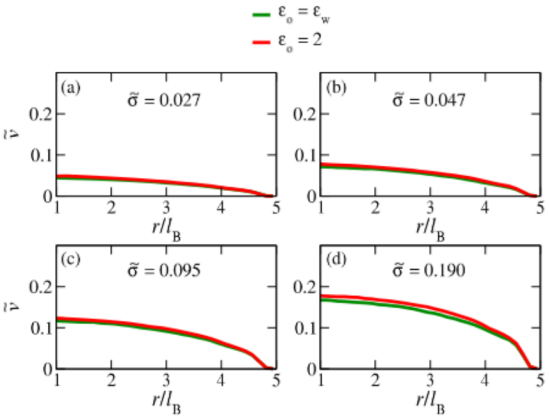

Figure 3. Fluid velocity profiles for the same parameters as shown in Figure 2. Green and red lines represent nonpolarizable and polarizable cases, respectively.

https://doi.org/10.1021/acs.jpcb.1c06783
J. Phys. Chem. B 2021, 125, 11091−11098

counterions at $N_c = 20$. The density profiles of trivalent counterions are presented in Figure 4. We see that, for

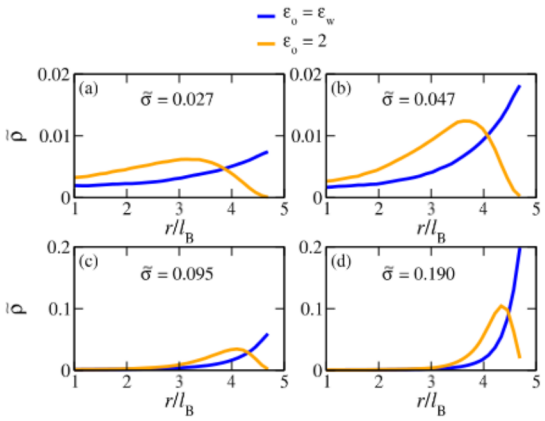

Figure 4. Trivalent counterion density profiles for pores of various surface charge densities. The periodic length L in each panel is $70l_B$, $40l_B$, $20l_B$, and $10l_B$, respectively, and the number of trivalent counterions inside one period is $N_c = 20$. The pore radius is $R/l_B = 5$. Blue and orange curves correspond to homogeneous (no dielectric discontinuity) and polarizable ($\varepsilon_w = 80$ and $\varepsilon_o = 2$) cases, respectively.

polarizable pores, trivalent counterions are strongly repelled from the surface. On the other hand, for homogeneous—nonpolarizable—pores with large surface charge density, the counterions are strongly attracted to the surface, as can be seen in Figure 4d. If an external electric field is applied along the major axis of the pore, we expect that the solvent velocity will be larger for polarizable pores than for homogeneous ones, since fewer ions will be near the surface of the pore, where they are affected by the no-slip boundary condition. The larger concentration of ions away from the surface of the pore will result in more collisions with the fluid particles and larger transfer of momentum. This is, indeed, what we observe in Figure 5. The fluid velocity at the center of a highly charged polarizable pore is almost three times that of an equivalent nonpolarizable pore. Note that ion velocity profiles inside polarizable and nonpolarizable pores are almost identical (see Figure 5e). Therefore, the increase in fluid velocity inside polarizable pores is a consequence of ion radial distribution.

The VFR can be calculated from the integral of the fluid velocity profile:

$$Q = 2\pi \int_0^R r v(r)\, \mathrm{d}r \tag{21}$$

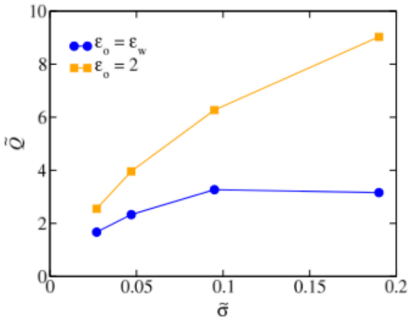

Figure 6. Volumetric flow rate as a function of charge density, comparing nonpolarizable and polarizable pores with trivalent counterions. The parameters are the same as in Figure 4.

The results for VFR are presented in Figure 6, using the reduced variable $\tilde{Q}$ ($\tilde{Q} = \sqrt{m\beta}\, Q/{l_B}^2$). We see that, for polarizable pores, VFR is significantly larger than for nonpolarizable pores. Furthermore, for homogeneous pores, the VFR saturates, while for polarizable pores, VFR monotonically increases with the pore surface charge. The saturation is analogous to Manning condensation found for linear polyelectrolytes.[57−59] The absence of saturation of VFR is a consequence of strong repulsion of multivalent ions from the polarizable surface, resulting in large ionic concentration in the bulk of the pore. These ions can more easily transfer their momentum to the fluid, since, in this region, the fluid is not affected by the no-slip boundary condition that prevents flow of the boundary layer.

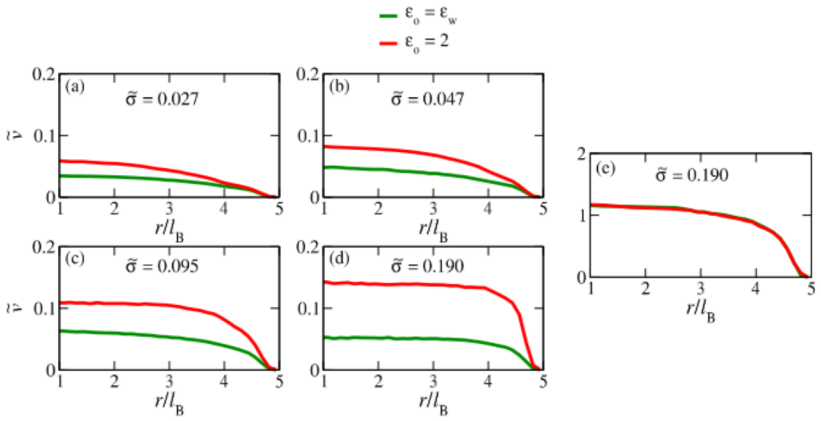

Figure 5. Panels (a−d): fluid velocity profiles for the same parameters as shown in Figure 4. Green and red lines represent nonpolarizable and polarizable cases, respectively. Panel (e) shows the velocity profiles of *counterions* for the same parameters as in panel (d). Note that the ion velocities are almost identical inside polarizable and nonpolarizable pores; the two curves overlap. Therefore, the increase in the fluid velocity for polarizable pores is due to the larger concentration of counterions *away* from the pore surface. These ions are not affected by the no-slip boundary condition, resulting in more momentum transfer between the ions and the fluid particles.

https://doi.org/10.1021/acs.jpcb.1c06783
J. Phys. Chem. B 2021, 125, 11091−11098

We next explore the dynamics inside pores, which, in addition to monovalent counterions derived from the dissociation of surface groups, also contain strong 3:1 electrolyte. In this case, we consider pores of radius $R/l_B = 10$ and surface charge density $\tilde{\sigma} = 0.159$, inside a simulation cell of length $L = 10l_B$. The solvent concentration is fixed at $l_B^3 n_s = 3$. The number of monovalent counterions is fixed at $N_c = 100$. The flow profiles are obtained for various reduced 3:1 salt concentrations, $\tilde{\rho}_s = l_B^3 \rho_s$ (see Figure 7). We see, in Figure 8, that VFR saturates for high salt concentrations for both polarizable and nonpolarizable pores. However, in the case of polarizable pores, the VFR is almost 100% higher than for nonpolarizable pores of the same parameters.

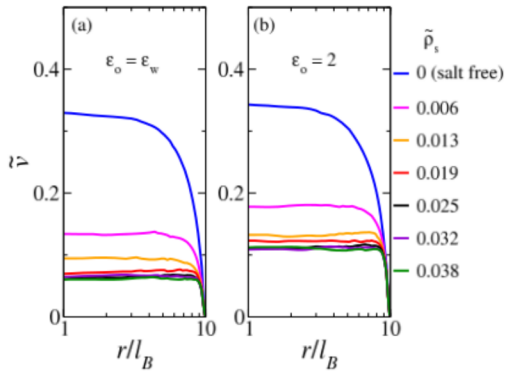

Figure 7. Fluid velocity profile inside (a) nonpolar and (b) polar pore of radius $R/l_B = 10$, containing $N_c = 100$ monovalent counterions and added 3:1 electrolyte at various concentrations, indicated on the right of the figure. These salt concentrations range from ~30 mM to 170 mM. The pore reduced surface charge density is $\tilde{\sigma} = 0.159$, corresponding to 49 mC/m^2.

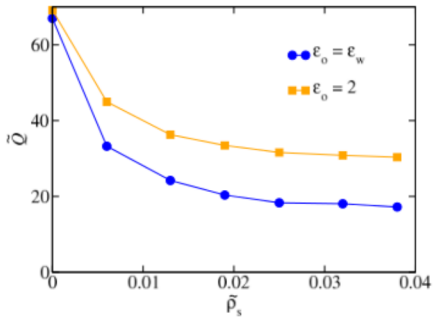

Figure 8. Volumetric flow rate, as a function of added 3:1 electrolyte concentration, for polarizable and nonpolarizable pores. The pore parameters are the same as in Figure 7.

CONCLUSIONS

We have presented a method to calculate the electrostatic energy of an electrolyte confined in a polarizable cylindrical pore. The method is applied to study the electroosmotic flow in charged nanopores. In this paper, we explored the effect of pore polarizability. It was found that polarization effects are very strong for systems with multivalent counterions, whereas, for systems with monovalent counterions, they are only marginally important. In the case of polarizable pores with only trivalent counterions, we find that VFR monotonically increases with the surface charge density, very different from what is observed for nonpolarizable pores for which VFR saturates with the pore surface charge. In the presence of 3:1 electrolyte, we find that, for parameters studied in the present work, the flow rate saturates with increasing salt concentration for both polarizable and nonpolarizable pores; however, in the case of polarizable pores, the flow rate is almost 100% higher, compared to that of nonpolarizable pores.

ASSOCIATED CONTENT

Supporting Information

The Supporting Information is available free of charge at https://pubs.acs.org/doi/10.1021/acs.jpcb.1c06783.

Derivation of the polarization force (PDF)

AUTHOR INFORMATION

Corresponding Authors

Rogério K. Bombardelli − *Instituto de Física, Universidade Federal do Rio Grande do Sul, 91501-970 Porto Alegre, RS, Brazil*; Email: rogerio.bombardelli@ufrgs.br

Igor M. Telles − *Instituto de Física, Universidade Federal do Rio Grande do Sul, 91501-970 Porto Alegre, RS, Brazil*; Email: igor.morais@ufrgs.br

Alexandre P. dos Santos − *Instituto de Física, Universidade Federal do Rio Grande do Sul, 91501-970 Porto Alegre, RS, Brazil*; orcid.org/0000-0002-5965-3992; Email: alexandre.pereira@ufrgs.br

Yan Levin − *Instituto de Física, Universidade Federal do Rio Grande do Sul, 91501-970 Porto Alegre, RS, Brazil*; orcid.org/0000-0002-0636-7300; Email: levin@if.ufrgs.br

Complete contact information is available at: https://pubs.acs.org/10.1021/acs.jpcb.1c06783

Notes

The authors declare no competing financial interest.

ACKNOWLEDGMENTS

This work was partially supported by CAPES, FAPERGS, INCT-FCx, and by the Brazilian Research Council (CNPq) under Grant No. 302720/2018-9.

REFERENCES

(1) Modi, N.; Winterhalter, M.; Kleinekathöfer, U. Computational modeling of ion transport through nanopores. *Nanoscale* **2012**, *4*, 6166−6180.

(2) Xiao, K.; Jiang, L.; Antonietti, M. Ion Transport in Nanofluidic Devices for Energy Harvesting. *Joule* **2019**, *3*, 2364−2380.

(3) Breitsprecher, K.; Janssen, M.; Srimuk, P.; Mehdi, B. L.; Presser, V.; Holm, C.; Kondrat, S. How to speed up ion transport in nanopores. *Nat. Commun.* **2020**, *11*, 6085.

(4) Ramirez, P.; Gomez, V.; Cervera, J.; Schiedt, B.; Mafe, S. Ion transport and selectivity in nanopores with spatially inhomogeneous fixed charge distributions. *J. Chem. Phys.* **2007**, *126*, 194703.

(5) Mei, L.; Yeh, L.-H.; Qian, S. Gate modulation of proton transport in a nanopore. *Phys. Chem. Chem. Phys.* **2016**, *18*, 7449−7458.

(6) Eisenberg, B. Ionic channels in biological membranes- electrostatic analysis of a natural nanotube. *Contemp. Phys.* **1998**, *39*, 447−466.

(7) Amiri, H.; Shepard, K. L.; Nuckolls, C.; Sanchez, R. H. Single-Walled Carbon Nanotubes: Mimics of Biological Ion Channels. *Nano Lett.* **2017**, *17*, 1204−1211.

(8) Simon, P.; Gogotsi, Y. Materials for Electrochemical Capacitors. *Nat. Mater.* **2008**, *7*, 845−54.

(9) Siria, A.; Poncharal, P.; Biance, A.-L.; Fulcrand, R.; Blase, X.; Purcell, S.; Bocquet, L. Giant osmotic energy conversion measured in a single transmembrane boron nitride nanotube. *Nature* **2013**, *494*, 455−8.
(10) Xiao, K.; Chen, L.; Jiang, L.; Antonietti, M. Carbon nitride nanotube for ion transport based photo-rechargeable electric energy storage. *Nano Energy* **2020**, *67*, 104230.
(11) Siwy, Z. S. Ion-Current Rectification in Nanopores and Nanotubes with Broken Symmetry. *Adv. Funct. Mater.* **2006**, *16*, 735−746.
(12) Zhu, Z.; Wang, D.; Tian, Y.; Jiang, L. Ion/Molecule Transportation in Nanopores and Nanochannels: From Critical Principles to Diverse Functions. *J. Am. Chem. Soc.* **2019**, *141*, 8658−8669.
(13) Feng, G.; Cummings, P. T. Supercapacitor Capacitance Exhibits Oscillatory Behavior as a Function of Nanopore Size. *J. Phys. Chem. Lett.* **2011**, *2*, 2859−2864.
(14) Jiang, D.-e.; Jin, Z.; Henderson, D.; Wu, J. Solvent Effect on the Pore-Size Dependence of an Organic Electrolyte Supercapacitor. *J. Phys. Chem. Lett.* **2012**, *3*, 1727−1731.
(15) Xiao, K.; Wan, C.; Jiang, L.; Chen, X.; Antonietti, M. Bioinspired Ionic Sensory Systems: The Successor of Electronics. *Adv. Mater.* **2020**, *32*, 2000218.
(16) Angeli, E.; Repetto, L.; Firpo, G.; Valbusa, U. Electrical biosensing with synthetic nanopores and nanochannels. *Curr. Opin. Electrochem.* **2021**, *29*, 100754.
(17) Duong-Hong, D.; Han, J.; Wang, J.-S.; Hadjiconstantinou, N.; Chen, Y.; Liu, G. R. Realistic simulations of combined DNA electrophoretic flow and EOF in nano-fluidic devices. *Electrophoresis* **2008**, *29*, 4880−6.
(18) Marbach, S.; Bocquet, L. Osmosis, from molecular insights to large-scale applications. *Chem. Soc. Rev.* **2019**, *48*, 3102−3144.
(19) Probstein, R. F.; Hicks, R. E. Removal of contaminants from soils by electric fields. *Science* **1993**, *260*, 498−503.
(20) Martin, L.; Alizadeh, V.; Meegoda, J. Electro-osmosis treatment techniques and their effect on dewatering of soils, sediments, and sludge: A review. *Soils Found.D* **2019**, *59*, 407−418.
(21) Manz, A.; Effenhauser, C. S.; Burggraf, N.; Harrison, D. J.; Seiler, K.; Fluri, K. Electroosmotic pumping and electrophoretic separations for miniaturized chemical analysis systems. *J. Micromech. Microeng.* **1994**, *4*, 257−265.
(22) Rathore, A.; Horváth, C. Capillary electrochromatography: theories on electroosmotic flow in porous media. *J. Chromatogr. A* **1997**, *781*, 185−195.
(23) Garcia, A. L.; Ista, L. K.; Petsev, D. N.; O'Brien, M. J.; Bisong, P.; Mammoli, A. A.; Brueck, S. R. J.; Lopez, G. P. Electrokinetic molecular separation in nanoscale fluidic channels. *Lab Chip* **2005**, *5*, 1271−1276.
(24) Moeendarbary, E.; Ng, T.; Pan, H.; Lam, K. Migration of DNA molecules through entropic trap arrays: A dissipative particle dynamics study. *Microfluid. Nanofluid.* **2010**, *8*, 243−254.
(25) Hatlo, M. M.; Panja, D.; van Roij, R. Translocation of DNA Molecules through Nanopores with Salt Gradients: The Role of Osmotic Flow. *Phys. Rev. Lett.* **2011**, *107*, 068101.
(26) Khodabandehloo, A.; Chen, D. D. Y. Electroosmotic Flow Dispersion of Large Molecules in Electrokinetic Migration. *Anal. Chem.* **2017**, *89*, 7823−7827.
(27) Harnett, C. K.; Templeton, J.; Dunphy-Guzman, K. A.; Senousy, Y. M.; Kanouff, M. P. Model based design of a microfluidic mixer driven by induced charge electroosmosis. *Lab Chip* **2008**, *8*, 565−572.
(28) Wang, X.; Cheng, C.; Wang, S.; Liu, S. Electroosmotic pumps and their applications in microfluidic systems. *Microfluid. Nanofluid.* **2009**, *6*, 145.
(29) Kirby, B. *Micro- and Nanoscale Fluid Mechanics: Transport in Microfluidic Devices*; Cambridge University Press, 2010.
(30) Leong, I. W.; Tsutsui, M.; Murayama, S.; He, Y.; Taniguchi, M. Electroosmosis-Driven Nanofluidic Diodes. *J. Phys. Chem. B* **2020**, *124*, 7086−7092.
(31) Arima, A.; Tsutsui, M.; Washio, T.; Baba, Y.; Kawai, T. Solid-State Nanopore Platform Integrated with Machine Learning for Digital Diagnosis of Virus Infection. *Anal. Chem.* **2021**, *93*, 215−227.
(32) Bratko, D.; Jönsson, B.; Wennerström, H. Electrical double layer interactions with image charges. *Chem. Phys. Lett.* **1986**, *128*, 449−454.
(33) Kanduč, M.; Podgornik, R. Electrostatic image effects for counterions between charged planar walls. *Eur. Phys. J. E: Soft Matter Biol. Phys.* **2007**, *23*, 265−74.
(34) dos Santos, A. P.; Levin, Y. Electrolytes between dielectric charged surfaces: Simulations and theory. *J. Chem. Phys.* **2015**, *142*, 194104.
(35) Shen, M.; Li, H.; de la Cruz, M. O. Surface Polarization Effects on Ion-Containing Emulsions. *Phys. Rev. Lett.* **2017**, *119*, 138002.
(36) dos Santos, A. P.; Girotto, M.; Levin, Y. Simulations of Coulomb Systems with Slab Geometry Using an Efficient 3D Ewald Summation Method. *J. Chem. Phys.* **2016**, *144*, 144103.
(37) dos Santos, A. P.; Girotto, M.; Levin, Y. Simulations of Coulomb systems confined by polarizable surfaces using periodic Green functions. *J. Chem. Phys.* **2017**, *147*, 184105.
(38) dos Santos, A. P.; Netz, R. R. Dielectric boundary effects on the interaction between planar charged surfaces with counterions only. *J. Chem. Phys.* **2018**, *148*, 164103.
(39) Petersen, B.; Roa, R.; Dzubiella, J.; Kanduč, M. Ionic structure around polarizable metal nanoparticles in aqueous electrolytes. *Soft Matter* **2018**, *14*, 4053−4063.
(40) Bagchi, D.; de la Cruz, M. O. Dynamics of a driven confined polyelectrolyte solution. *J. Chem. Phys.* **2020**, *153*, 184904.
(41) dos Santos, A. P.; Bakhshandeh, A.; Levin, Y. Effects of the dielectric discontinuity on the counterion distribution in a colloidal suspension. *J. Chem. Phys.* **2011**, *135*, 044124.
(42) Zwanikken, J. W.; de la Cruz, M. O. Tunable soft structure in charged fluids confined by dielectric interfaces. *Proc. Natl. Acad. Sci. U. S. A.* **2013**, *110*, 5301−5308.
(43) Bagchi, D.; Nguyen, T. D.; de la Cruz, M. O. Surface polarization effects in confined polyelectrolyte solutions. *Proc. Natl. Acad. Sci. U. S. A.* **2020**, *117*, 19677−19684.
(44) Tergolina, V. B.; dos Santos, A. P. Effect of dielectric discontinuity on a spherical polyelectrolyte brush. *J. Chem. Phys.* **2017**, *147*, 114103.
(45) Yuan, J.; Antila, H. S.; Luijten, E. Dielectric Effects on Ion Transport in Polyelectrolyte Brushes. *ACS Macro Lett.* **2019**, *8*, 183−187.
(46) Levin, Y. Electrostatic Correlations: from Plasma to Biology. *Rep. Prog. Phys.* **2002**, *65*, 1577−1632.
(47) Palaia, I.; Telles, I. M.; dos Santos, A. P.; Trizac, E. Electroosmosis as a probe for electrostatic correlations. *Soft Matter* **2020**, *16*, 10688−10696.
(48) Telles, I. M.; dos Santos, A. P. Electroosmotic Flow Grows with Electrostatic Coupling in Confining Charged Dielectric Surfaces. *Langmuir* **2021**, *37*, 2104−2110.
(49) Daub, C. D.; Cann, N. M.; Bratko, D.; Luzar, A. Electrokinetic flow of an aqueous electrolyte in amorphous silica nanotubes. *Phys. Chem. Chem. Phys.* **2018**, *20*, 27838−27848.
(50) Solis, F. J.; de la Cruz, M. O. Pimples reduce and dimples enhance flat dielectric surface image repulsion, arXiv2105.14392, 2021.
(51) Telles, I. M.; Bombardelli, R. K.; dos Santos, A. P.; Levin, Y. Simulations of electroosmotic flow in charged nanopores using Dissipative Particle Dynamics with Ewald summation. *J. Mol. Liq.* **2021**, *336*, 116263.
(52) Groot, R. D.; Warren, P. B. Dissipative particle dynamics: Bridging the gap between atomistic and mesoscopic simulation. *J. Chem. Phys.* **1997**, *107*, 4423−4435.
(53) Español, P.; Warren, P. Statistical Mechanics of Dissipative Particle Dynamics. *Europhys. Lett.* **1995**, *30*, 191−196.
(54) Español, P. Hydrodynamics from dissipative particle dynamics. *Phys. Rev. E: Stat. Phys., Plasmas, Fluids, Relat. Interdiscip. Top.* **1995**, *52*, 1734−1742.

https://doi.org/10.1021/acs.jpcb.1c06783
J. Phys. Chem. B 2021, 125, 11091−11098

(55) Pivkin, I.; Karniadakis, G. A new method to impose no-slip boundary conditions in dissipative particle dynamics. *J. Comput. Phys.* **2005**, *207*, 114−128.
(56) Levin, Y. Electrostatics of ions inside the nanopores and transmembrane channels. *Europhysics Letters (EPL)* **2006**, *76*, 163−169.
(57) Engstrom, S.; Wennerström, H. Ion condensation on planar surfaces. A solution of the Poisson-Boltzmann equation for two parallel charged plates. *J. Phys. Chem.* **1978**, *82*, 2711−2714.
(58) Manning, G. S. Counterion Condensation on Charged Spheres, Cylinders, and Planes. *J. Phys. Chem. B* **2007**, *111*, 8554−8559.
(59) Jabes, B. S.; Bratko, D.; Luzar, A. Curvature dependence of the effect of ionic functionalization on the attraction among nanoparticles in dispersion. *J. Chem. Phys.* **2018**, *148*, 222815.

https://doi.org/10.1021/acs.jpcb.1c06783
J. Phys. Chem. B 2021, 125, 11091−11098